2026 IEEE International Conference on Robotics and Automation (ICRA 2026)
June 1-5, 2026. Vienna, Austria

# Robust Friction Estimation for an Active Upper-Limb Exoskeleton via SOSML Observer

Hamidreza Heidari, Paolino De Risi, and Fanny Ficuciello

*Abstract*— **Friction in compact, geared actuators remains a primary barrier to transparency in upper-limb exoskeletons, especially near zero velocity and during frequent reversals. A momentum-based estimation framework is developed and evaluated on a two-DoF active device (modified EDUExo), where joint friction is recovered from on-board joint measurements and fitted to Coulomb–viscous and Stribeck laws. Two estimators are compared under identical conditions: a first-order momentum observer (FO) and a second-order sliding-mode momentum observer (SOSML). Three velocity trajectories are designed to probe complementary behaviors. In simulation, SOSML adheres more closely to the S-shaped friction law, and preserves loop symmetry under encoder noise; parameter variance and robustness under structured model mismatch are likewise improved relative to FO. The results indicate that SOSML delivers lower lag, cleaner noise profiles, and reduced parameter drift without changing the signal set or adding sensors, thereby strengthening friction identification and compensation on compact, gear-reduced actuators.**

## I. Introduction

Human–exoskeleton systems are required to exhibit low apparent impedance, smooth motion near zero speed, and predictable interaction forces; yet unmodeled joint friction has been shown to undermine all three by reducing back drivability, inducing stick–slip in the Stribeck region, and corrupting torque tracking, with adverse effects on comfort, safety, and transparency for the wearer [1]. The challenge is exacerbated in compact, gear-reduced actuators that are common in wearable robots, where friction and cogging effects are pronounced and vary with operating conditions.

Foundational descriptions of friction have been provided through dynamic models that compactly capture velocity weakening and pre-sliding behavior while retaining interpretable parameters. In particular, the LuGre formulation has been employed to represent Coulomb, viscous, and Stribeck phenomena and to support parameter identification and feedforward compensation in robotic joints; its structure has enabled practical excitation design around the low-speed regime and systematic controller integration [2]. Nonlinear joint friction remains a primary barrier to precision force/position control in robotics—especially in adaptive grinding—because classical Coulomb–viscous/Stribeck laws and static, steady-state identification fail to capture the presliding–sliding transition and yield biased compensation [3].

To reduce reliance on explicit friction parameterization, direct friction observers have been introduced and validated. In robots equipped with joint torque sensing, online reconstruction of friction has been demonstrated and used for compensation, with improvements reported in joint positioning and torque control; such evidence has established observer-based friction handling as a feasible and effective option in joint-level servo loops [4].

In parallel, disturbance/momentum observer frameworks have been developed in which all unmodeled torques—including friction—are treated as lumped disturbances and estimated sensor-lessly from the robot dynamics and proprioceptive measurements. The disturbance-observer (DOB) paradigm has been consolidated over decades and deployed widely in robust motion control for precision actuation, offering a unifying perspective and practical synthesis rules [5]. Within robotics, momentum-observer formulations have linked residuals to external torques and have been employed extensively for interaction monitoring and collision detection; at the same time, the bandwidth–noise trade-off and asymptotic accuracy (for piecewise constant disturbances) of first-order designs have been documented and discussed [6], [7].

However, each strand above entails specific limitations, explicit friction models can be operating-point sensitive and may not capture pre-sliding dynamics adequately; torque-sensor-based observers introduce hardware, calibration, and noise sensitivities; and first-order DOB/momentum observers face the fundamental bandwidth–noise compromise and only asymptotically reject low-frequency disturbances [8]. To mitigate these limitations, sliding-mode observers have been advanced. Second-order sliding (super-twisting) designs have been analyzed via Lyapunov methods, and finite-time convergence of estimation errors has been established under mild regularity assumptions, thereby reducing phase lag without resorting to very high observer bandwidths that would amplify sensor noise [9]. Building on this theory, sliding-mode momentum observers have been proposed for robots to estimate external torques (and even joint accelerations) with enhanced robustness to modeling errors and measurement noise relative to first-order momentum observers, indicating

H. Heidari is with Technische Hochschule Deggendorf, Lehrcampus Cham, 93413 Cham, Germany (corresponding author, e-mail: hamidreza.heidari@th-deg.de).

P. De Risi and F. Ficuciello are with Department of Electrical Engineering, Università degli Studi di Napoli Federico II, 80125 Naples, Italy.

strong potential for friction-oriented disturbance reconstruction [10].

Observer concepts have also been adapted to wearable devices to contend with friction and model uncertainties while maintaining transparency. Extended-state observer (ADRC-style) schemes have been applied to lower-limb exoskeletons to estimate lumped disturbances online and to preserve trajectory tracking in the presence of unknown loads and parameter variations [11]. In related efforts, nonlinear disturbance observers have been combined with backstepping sliding-mode control in knee assistance, and disturbance-compensating strategies have been investigated for human–exoskeleton systems to attenuate load-torque effects—collectively underscoring the practicality of observer-based uncertainty handling in wearable actuation [12], [13].

Against this background, friction estimation is posed here as a disturbance-estimation problem on an active two-motor upper-limb exoskeleton (modified EDUExo). A head-to-head comparison is conducted between a first-order momentum observer and a sliding-mode momentum observer of the SOSML type, with emphasis placed on low-speed behavior in the Stribeck region. A set of three speed trajectories (low/medium/high) is designed to probe near-zero velocity while respecting actuator limits, and a two-stage evaluation is performed: simulations with injected sensor noise and structured model mismatch, followed by hardware experiments in which Coulomb/viscous/Stribeck parameters are identified from the observer output. In this way, an evidence-based assessment is provided of the extent to which sliding-mode momentum estimation can deliver lower lag, improved robustness, and faster convergence for friction identification in wearable exoskeleton joints, relative to a strong linear baseline.

## II. System Description

### A. Architecture and actuation

The platform is configured as a planar 2-DoF upper-limb exoskeleton with revolute shoulder and elbow joints and rigid upper-arm/forearm links mechanically coupled to a solid human-arm model. The assembly is realized in CAD and imported into Simscape Multibody so that masses, inertias, frames, and joint constraints are preserved; this enables coupled human–robot dynamics to be simulated with consistent reaction forces and joint behavior. Actuation is provided by an RMD-X6 drive at the shoulder and a servo at the elbow, with proprioceptive sensing for joint states (and motor-side signals when available). This stack supplies the state/torque signals needed for model-based analysis and later observer-based friction estimation, without external force/torque sensors. Figure 1 depicts a schematic representation of the planar two-link configuration used throughout the study.

### B. Kinematics and dynamics formulation

The kinematic modeling of the exoskeleton involves determining the relationship between the joint variables and the position and velocity of the end-effector. In the forward kinematics analysis, the position of the end-effector (i.e., the hand) is expressed as a function of the joint angles $\theta_1$ and $\theta_2$. The endpoint position is first calculated in the local plane and then rotated into the global workspace using a 20° rotation matrix about the x-axis:

$$\boldsymbol{p}_{end} = R_x(20°).\begin{bmatrix} l_1 cos(\theta_1) + l_2 cos(\theta_1 + \theta_2) \\ l_1 sin(\theta_1) + l_2 sin(\theta_1 + \theta_2) \\ 0 \end{bmatrix} \quad (1)$$

Where $l_1$ and $l_2$ are the lengths of the upper arm and forearm links, respectively and $R_x(20°)$ is the rotation matrix applied to align the coordinate system with the real-world shoulder inclination. This formulation allows the controller to map desired end-effector trajectories into joint space while accounting for the inclination.

To perform inverse kinematics, the goal is to find joint angles $\theta_1$ and $\theta_2$ that position the end-effector at a desired location in space. The inverse kinematics equations are derived analytically (when feasible) or solved numerically in Simulink using optimization or iterative solvers. Because the workspace is inclined, the desired position vector $\boldsymbol{p}_{desired}$ is first transformed into the local coordinate system using the inverse of the original rotation:

$$\boldsymbol{p}_{local} = R_x(-20°) \cdot \boldsymbol{p}_{desired} = [x' \quad y' \quad z']^T \quad (2)$$

Then, the inverse kinematics is computed using standard geometric relationships in the local plane:

$$\begin{aligned} cos(\theta_2) &= \frac{x'^2 + y'^2 - {l_1}^2 - {l_2}^2}{2 l_1 l_2} \\ \theta_1 &= tan^{-1}\left(\frac{y'}{x'}\right) - tan^{-1}\left(\frac{l_2 sin(\theta_2)}{l_1 + l_2 cos(\theta_2)}\right) \end{aligned} \quad (3)$$

The solution is straightforward and must be constrained to feasible human-safe joint limits to ensure anatomical realism and avoids singularities.

The dynamic behavior of the exoskeleton is formulated using the Lagrangian method, which offers a structured approach for deriving the equations of motion. The kinetic energy of each link is expressed in terms of the generalized joint coordinates and velocities, accounting for the rotational inertia and linear velocities of both the center of mass and distal end. The potential energy is computed based on the vertical position of each center of mass, adjusted to reflect the inclined gravitational vector due to the 20° coordinate frame rotation.

The Lagrangian $\boldsymbol{L}$ is defined as the difference between total kinetic and potential energies:

$$\boldsymbol{L} = T - V \quad (4)$$

By considering $m_1, m_2$ the masses of the upper arm and forearm links, $I_1, I_2$ their moments of inertia, and $l_1, l_2$ their lengths. Let $c_1, c_2$ denote the distances from the respective joints to the centers of mass. The total kinetic energy is given by:

$$T = \frac{1}{2} I_1 \dot{\theta}_1^2 + \frac{1}{2} m_1 c_1^2 \dot{\theta}_1^2 + \frac{1}{2} I_2 \left(\dot{\theta}_1 + \dot{\theta}_2\right)^2 + \frac{1}{2} m_2 \left[v_{c2x}^2 + v_{c2y}^2\right] \quad (5)$$

where $v_{c2x} = -l_1 \dot{\theta}_1 sin(\theta_1) - c_2\left(\dot{\theta}_1 + \dot{\theta}_2\right) sin(\theta_1 + \theta_2)$ and $v_{c2y} = l_1 \dot{\theta}_1 cos(\theta_1) + c_2\left(\dot{\theta}_1 + \dot{\theta}_2\right) cos(\theta_1 + \theta_2)$

The projected point due to 20° inclination, the gravity vector **g** is rotated as:

$$\mathbf{g} = R_x(20°) \cdot \begin{bmatrix} 0 \\ -g \\ 0 \end{bmatrix} = \begin{bmatrix} 0 \\ -g cos(20°) \\ g sin(20°) \end{bmatrix} \quad (6)$$

Only the vertical (y and z) components contribute to the potential energy. Assuming motion is constrained to a plane and z-component affects height slightly, the potential energy becomes:

$$\mathbf{V} = \left(m_1 g c_1 cos(\theta_1) + m_2 g \left[l_1 cos(\theta_1) + c_2 cos(\theta_1 + \theta_2)\right]\right) cos(20°) \quad (7)$$

This yields the system's equations in the standard robotic form:

$$M(q)\ddot{q} + C(q, \dot{q})\dot{q} + G(q) = \tau \quad (8)$$

The dynamic model includes the inertia matrix $M(q)$, Coriolis and centrifugal forces $C(q, \dot{q})$, gravity effects $G(q)$ and the torque vector $\tau$. Simulink is used to simulate the system under various strategies, while Simscape provides visual and numerical validation of the derived kinematics and dynamics.

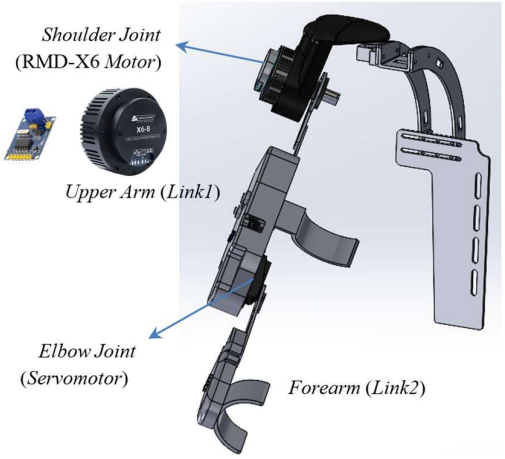


Figure 1. Schematic representation of the 2-link upper-limb exoskeleton (shoulder–elbow).

## III. Estimation Methods

This section describes the friction models and observer-based estimation used in our study. Standard Coulomb–viscous and Stribeck forms are adopted to represent joint friction, while momentum-based observers are employed to estimate the lumped disturbance that is dominated by friction. Parameters are identified from velocity–disturbance data using constrained fits with basic physical and symmetry checks.

### A. Friction models for identification

Joint friction is modeled for identification using two standard forms. The first is the Coulomb–viscous law

$$\tau_f(\dot{q}) = C_f \, \mathrm{sgn}(\dot{q}) + V_f \, \dot{q} \quad (9)$$

with $C_f \geq 0$ and $V_f \geq 0$. To account for low-speed weakening, a Stribeck extension is employed,

$$\tau_f(\dot{q}) = C_f \, \mathrm{sgn}(\dot{q}) + V_f \, \dot{q} + S_f \exp[-(|\dot{q}|/\lambda)^{\alpha}] \, \mathrm{sgn}(\dot{q}) \quad (10)$$

with $S_f \geq C_f \geq 0$, $\lambda \geq 0$ and $\alpha \in [1,2]$. Physically, $C_f$ represents the constant Coulomb friction opposing motion, while $V_f$ captures the linear viscous drag prevalent at higher speeds. The Stribeck parameters specifically model the low-speed regime: $S_f$ dictates the magnitude of the breakaway friction peak, $\lambda$ defines the threshold velocity for the stick-slip transition, and $\alpha$ shapes the decay curve. During contact-free tests, the disturbance estimate $\hat{\tau}_e$ provided by the observers is interpreted as friction, and parameters $\{C_f, V_f\}$ or $\{C_f, V_f, S_f, \lambda, \alpha\}$ are obtained by constrained least-squares fits on $(\dot{q}, \hat{\tau}_e)$ data. Symmetry constraints around $\dot{q} = 0$ and inspection of odd/even components are used to check plausibility of the identified models.

### B. Momentum-based observers

Two observer structures are used to estimate the lumped disturbance $\tau_e$ that, under the trajectories considered, is dominated by joint friction. As a baseline, a compact first-order momentum observer is adopted by introducing an auxiliary state $z \in \mathbb{R}^2$ and updating it together with the disturbance estimate $\hat{\tau}_e \in \mathbb{R}^2$ according to

$$\dot{z} = c_0 \hat{\tau}_e + c_0 (C(q, \dot{q}) - G(q) + \tau), \quad (11)$$

$$\hat{\tau}_e = k_0 \, M(q)\dot{q} - z, \quad (12)$$

where $k_0 > 0$ and $c_0 > 0$ are diagonal design gains. Eqs. (11)– (12) can be viewed as a first-order residual filter whose effective pole is shaped primarily by $c_0$, while $k_0$ sets the tracking gain on momentum.

By contrast, to reduce phase lag and improve robustness to noise and model mismatch, a second-order sliding construction with linear augmentation is used. Defining the momentum estimation error

$$\tilde{p} = \hat{p} - p, \qquad p = M(q)\dot{q}, \quad (13)$$

and use a smooth sign function to regularize the switching action,

$$s_\varepsilon(x) = \begin{cases} \mathrm{sgn}(x), & |x| > \varepsilon, \\ x/\varepsilon, & |x| \leq \varepsilon, \end{cases} \quad (14)$$

applied elementwise with a small $\varepsilon > 0$. The SOSML dynamics are then

$$\dot{\hat{p}} = \tau + C(q, \dot{q})\dot{q} - G(q) - T_1 \left(\sqrt{|\tilde{p}|}.s_\varepsilon(\tilde{p})\right) - T_2 \, \tilde{p} + \hat{\tau}_e, \quad (15)$$

$$\dot{\hat{\tau}}_e = -S_1 s_\varepsilon(\tilde{p}) - S_2 \, \tilde{p}, \quad (16)$$

with diagonal gain matrices $T_1, T_2, S_1, S_2 > 0$ (joint-wise tuning). Intuitively, the super-twisting mechanism improves upon the first-order design by integrating the high-frequency switching of the sign function. This produces a continuous equivalent control signal that effectively filters measurement noise while maintaining finite-time convergence to the sliding surface, thereby reducing phase lag without amplifying sensor noise. A practical initialization is to select $S_1$ from an upper bound on the expected disturbance slope, set $T_1 \approx 1.6\sqrt{S_1}$ for near-optimal super-twisting transients [10], and choose $T_2, S_2$ to introduce light linear damping of $\tilde{p}$ without masking finite-time behavior.

## IV. Simulation Study

A planar 2-DoF shoulder–elbow plant is exercised to benchmark two disturbance observers, the first-order residual filter (FO) in equations (11)- (12) and the super-twisting sliding-mode observer (SOSML) in equations (15)- (16), under identical inputs $(q, \dot{q}, \tau)$, the same $(M, C, G)$, and matched numerical stepping. External contacts were disabled so that the disturbance $\tau_e$ is dominated by joint friction, and identification proceeded by fitting the observers' outputs $\hat{\tau}_e$ to the friction laws (9)- (10). Two excitation families were used: (i) a slow S-shaped motion that accelerates with a half fifth-order profile, dwells at a small constant velocity, and decelerates to rest, and (ii) a reversal motion in which joint 1 oscillates sinusoidally about a bias, producing regular direction changes. Each trajectory was run in three conditions: Nominal (no injected imperfections), Noise (zero-mean encoder noise added before numerical differentiation), and Mismatch (structured perturbations of $M(q)$ and small offsets in $G(q)$); neither observer was given model compensation beyond its own structure.

Figure 2 focuses on the slow S-shape at the most informative speeds for Stribeck identification, restricting the phase plane to $|\dot{q}_1| \leq 0.052$ rad/s. In these phase-plane plots, the raw scatter points correspond to the real-time observer estimates $(\dot{q}, \hat{\tau}_e(t))$ calculated during the dynamic motion. The smooth, overlaid lines represent the offline curve-fitting of these points using the defined Stribeck friction model. This distinction clarifies the relationship between the instantaneous observer behavior and the idealized steady-state friction map.

Around the zero crossing, SOSML follows the S-shaped friction transition more tightly and preserves symmetry about $\dot{q}_1 = 0$, while FO exhibits a visibly wider loop and a small phase lag in the stick–slip shoulder. On the constant-velocity plateau and during the final hold, the SOSML fit remains closer to the measured envelope, whereas the FO fit shows a slightly delayed approach to the Coulomb level. This figure captures the core low-speed contrast: SOSML reduces bias and lag where the Stribeck effect is strongest, without altering the signal set.

Noise sensitivity is summarized in Figure 3, which examines noise robustness by plotting time-domain errors (observer output minus the ideal friction model) for both trajectories. In the slow S-shape with noise (top panel), the FO trace forms a thick band with frequent spikes, whereas the SOSML error remains narrow and visibly contained. The annotated RMSE values quantify the gap. The same pattern appears for the reversal with noise (bottom panel): FO exhibits larger excursions and broader variance, while SOSML maintains a tight error tube; the RMSE annotations again favor SOSML. Because both observers share the same signals and gains are kept comparable, these traces highlight SOSML's better noise shaping: it preserves transient sharpness around reversals but transmits substantially less mid–high-frequency content to $\hat{\tau}_e$.

Robustness to model errors is probed in Figure 4, which probes robustness under model mismatch on the reversal trajectory. The top panel shows the phase-plane overlay of $\hat{\tau}_e$ vs. $\dot{q}$ with the fitted friction curves. Under perturbed dynamics, FO develops a wider loop and a noticeable distortion near the stick–slip shoulder; SOSML remains closer to an S-shape and keeps a tighter tube around its fit. The bottom panel compares the fitted parameters $[C_f, V_f, S_f, \lambda]$ against an ideal column. Consistent with the phase-plane view, SOSML recovers the viscous coefficient $V_f$ and the Stribeck smoothing $\lambda$ more faithfully (close to the ideal values), whereas FO tends to over-damp $V_f$ and collapse $\lambda$ toward zero. For the Coulomb level $C_f$, FO is slightly closer in this run, while both methods under-estimate $S_f$ (SOSML being nearer to the ideal than FO). Overall, SOSML's parameter set clusters nearer to the ideal in three of the four terms and, together with the tighter loop above, indicates reduced sensitivity to moderate plant mismatch.

Overall, the two trajectories reveal complementary aspects of performance. The slow S-shape isolates low-speed behavior and shows that SOSML adheres more closely to the Stribeck law right where identification is hardest, with less phase lag and smaller plateau error. The reversal isolates finite-time behavior and noise: SOSML returns to the identification band quickly after each direction change and maintains a markedly smaller error envelope under measurement noise. Under mismatch, the phase-plane loop and the parameter bars show SOSML retaining the overall friction shape and parameter set more reliably, while FO requires higher effective gains to match transients—at the cost of noisier steady-state estimates. Across all views, the advantage of SOSML is obtained without adding sensors or changing the excitation; it arises purely from the observer dynamics.

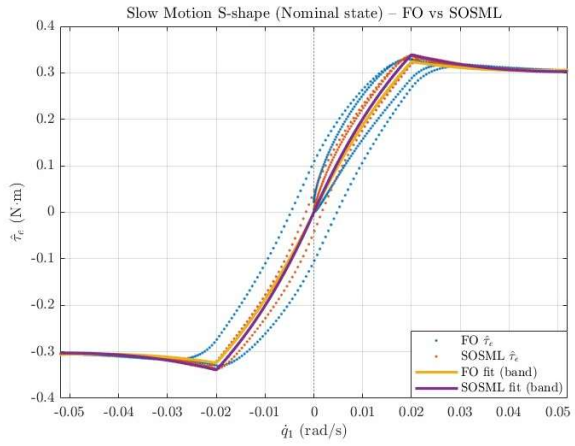


Figure 2. Slow Motion S-shape (Nominal State). FO and SOSML disturbance estimate versus $\dot{q}$.

## V. V. Experimental Evaluation

This section reports a hardware study on a wearable two-DoF upper-limb exoskeleton. All quantitative results refer to the shoulder joint. The objective is to compare two proprioception-only disturbance observers—the first-order residual (FO) and the second-order super-twisting momentum observer (SOSML)—as sources of data for identifying a Stribeck-type friction law directly from raw experimental signals. The sensing path is deliberately minimal: joint positions and velocities come from embedded encoders; motor current is mapped to joint torque through the measured torque constant and transmissions; and the same nominal rigid-body model terms are supplied to both observers. No additional filtering is applied in the figures or the metrics.

To make identification robust and fair, a very small velocity band around zero is excluded to remove the immediate reversal transient; steady windows are detected with a median-smoothed velocity; segment edges are trimmed (more aggressively for short half-cycles); and the Stribeck law is fitted using segment medians of the pairs $(\omega, \tau_e)$ with a Huber loss and light regularization on $\lambda$ and $\tau_{bias}$:

$$\tau_f(\dot{q}) = \operatorname{sgn}(\dot{q})[C + B\,|\dot{q}| + S\exp(-|\dot{q}|/v_s)] + \tau_{bias}, \quad (17)$$

The identical pipeline is applied to FO and to SOSML.

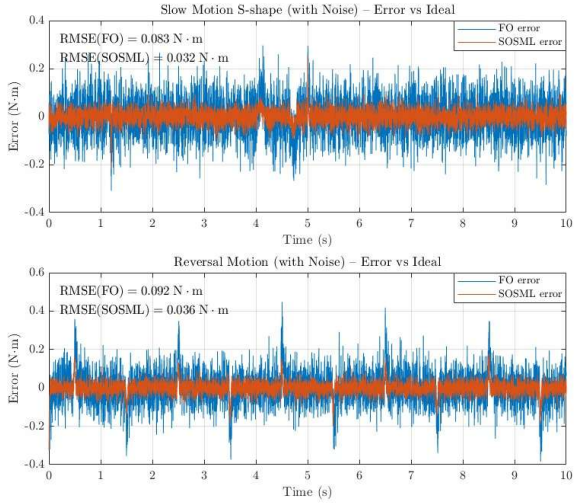


Figure 3. Noise robustness. Time-domain error traces for the slow S-shape (top) and reversal (bottom).

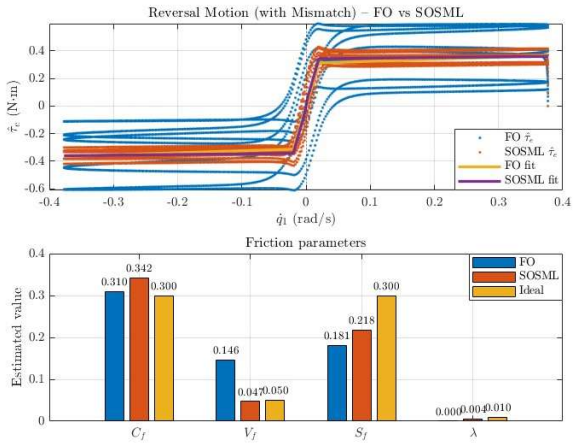


Figure 4. Reversal Motion with model mismatch. Top: phase-plane $\hat{\tau}_e$ vs. $\dot{q}$ with FO/SOSML fits. Bottom: grouped friction parameters $[C_f, V_f, S_f, \lambda]$ vs. ideal.

### A. Setup and protocol

Three complementary shoulder-joint trajectories expose the friction map over the operating range. Trajectory 1 (T1, "speed ladder") consists of S-curve ramps that connect long steady-velocity plateaus at incrementally increasing and then decreasing speeds (Figure 5, Top). These repeated quasi-constant-velocity windows are ideal for estimating the Coulomb term C and the viscous coefficient B with low variance. Trajectory 2 (T2, "symmetric reversal") is a train of short half-cycles centered near omega ≈ 0; it concentrates samples at the low-speed knee and is therefore most informative about the Stribeck amplitude S and the decay rate lambda (Figure 5, Bottom). Trajectory 3 (T3, "slow ladder") is a slower ladder with extended low-speed plateaus in both directions; it reinforces the steady terms and is especially useful for a stable estimate of the bias offset $\tau_{bias}$.

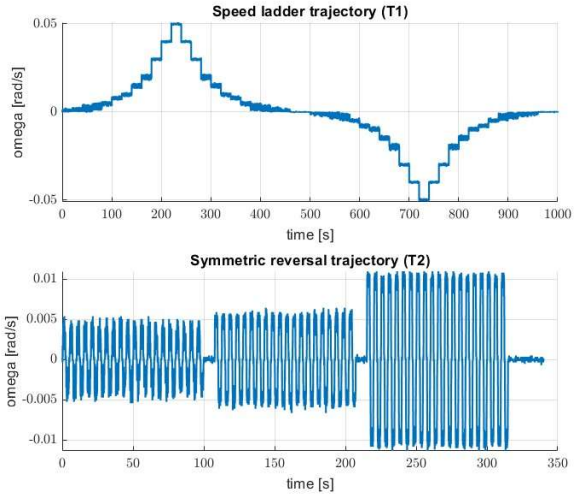


Figure 5. Trajectory overview. Top: speed ladder trajectory (T1). Bottom: symmetric reversal trajectory (T2).

*B. Results and discussion*

Figure 6 presents the S-shape scatter and fitted Stribeck curves for T1 (top) together with the identified parameter bars (bottom). Away from the origin, the two observers produce nearly identical viscous branches; the FO and SOSML clouds collapse onto the same lines and the fitted curves overlap. This indicates that either observer supports accurate recovery of C and B when good plateaus are available. Near omega = 0, SOSML produces a visibly tighter cloud and its medians on both sides of the origin align more symmetrically, whereas FO shows a small delay across reversals. Because the identification pipeline uses a tiny zero-band exclusion and median statistics, the knee fit remains stable for both observers on T1, but the SOSML knee exhibits less scatter.

Figure 7 applies the same visualization to T2, which concentrates data near the origin through frequent reversals. The advantage of SOSML is clearer here. As omega crosses zero, the SOSML loop remains narrow and centered, while FO exhibits a small but systematic lag that widens the loop around the origin. A least-squares fit on raw samples would be biased by this lag; the robust fitter and zero-band exclusion mitigate the effect, but the residual dispersion in S and lambda is still larger for FO. This behavior matches the design intent of the sliding-mode structure: SOSML rejects measurement ripple while retaining a sharp response to sign changes, which directly improves identifiability of the low-speed knee.

Trajectory 3, although not plotted, completes the picture. Its very long low-speed plateaus make the Coulomb and viscous estimates extremely repeatable and, importantly, provide a reliable value for the bias offset once the immediate reversal tail is trimmed. Across our runs, T1 and T3 produced highly consistent steady parameters for both observers. Typical medians placed C close to 0.26 Nm and B close to $2.5\times10^{-3}$ N.m.s/rad; the bias $\tau_{bias}$ was small but non-negligible at low speed, with representative values near 0.43 *N.m* depending on trajectory and observer. These steady values were essentially identical for FO and SOSML once the same segment selection and trimming were applied, confirming that both observers furnish plateau data of comparable quality.

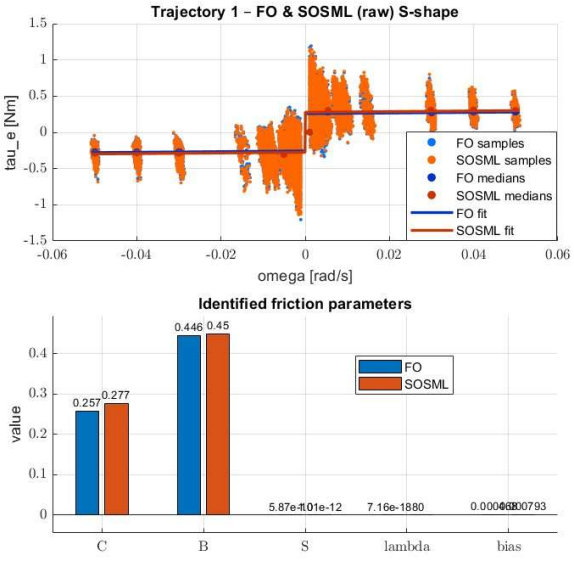


Figure 6. Trajectory 1 (T1): S-shape and parameters. Top: (omega, $\tau_e$) scatter for FO (blue) and SOSML (orange), segment medians (larger dots), and Stribeck fits (solid lines). Bottom: identified parameters (C, B, S, lambda, $\tau_{bias}$) for FO and SOSML.

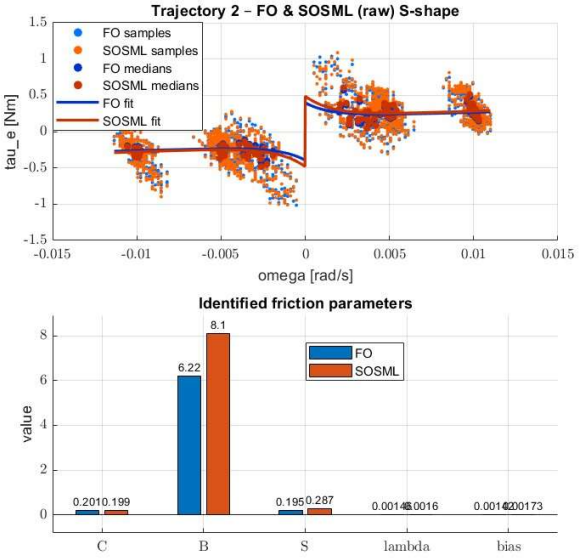


Figure 7. Trajectory 2 (T2): S-shape and parameters. Top: ($\omega$, $\tau_e$) scatter and fits focused on frequent reversals. Bottom: identified parameters.

The knee parameters are best determined from T2. Using the SOSML medians through the reversals, the Stribeck amplitude and decay rate concentrated at S ≈ 7.2 Nm and lambda ≈ $2.5\times10^{-3}$ rad/s. FO produced similar means but with noticeably larger spread due to its slightly wider origin loop. Because the knee is shaped by very low velocities, the observer dynamics dominate this part of the dataset; the tighter SOSML loop translates directly into more confident S and lambda.

Combining the evidence from the three trajectories, we form a single friction model by selecting each parameter from the trajectory—and the observer—that estimates it most

reliably. The plateaus in T1 and T3 fix C and B; the reversals in T2 fix S and lambda; the slow plateaus in T3 fix $\tau_{bias}$. To maintain consistency and to capitalize on the tighter low-speed behavior, we take the SOSML medians as our official values. The consolidated parameter vector, in SI units, is:

(C*, B*, S*, lambda*, $\tau_{bias}$*) = (0.26, $2.5\times10^{-3}$, 7.2, $2.5\times10^{-3}$, 0.43), with units (*N.m*, N.m.s/rad, *N.m*, rad/s, *N.m*). These values reproduce the S-shapes seen in Figures 2 and 3 across all excitations, yielding overlapping viscous branches at higher speeds and a narrow, symmetric origin crossing.

In summary, both observers are interchangeable on steady plateaus and lead to the same Coulomb and viscous terms. The decisive difference appears near zero velocity: SOSML consistently yields cleaner medians and tighter S-knee parameters, which is the practically important region for perceived transparency and for high-quality friction feedforward. Because the pipeline runs on raw proprioceptive signals with identical preprocessing for both observers, the differences observed here are attributable to the observer structure rather than to filtering or segmentation artifacts. For all subsequent use in our control experiments, we therefore adopt the consolidated friction model above and select SOSML values as the final friction parameters, while retaining FO as a simple and effective baseline for plateau-based monitoring.

## VI. Conclusion

A direct comparison of momentum observers for joint friction estimation was performed in both simulation and hardware on a upper-limb exoskeleton. Treating the observer residual as friction and fitting standard models enabled a matched-conditions evaluation under nominal operation, sensor noise, and model mismatch. The sliding-mode (SOSML) observer consistently delivered narrower friction loops, faster and more repeatable settling after reversals, and smaller variance in identified Stribeck parameters, while retaining parity with a first-order baseline at higher speeds. Crucially, these advantages arise without additional sensors and with modest computational cost, making deployment at control rates feasible on wearable platforms, as well as in highly constrained domains like surgical robotics. In teleoperated surgical systems, where compact, gear-reduced actuators are prevalent, avoiding the need for bulky, sterilization-sensitive external torque sensors while preserving joint-level force estimation is a significant advantage. The findings indicate that SOSML provides a more favorable accuracy–lag–robustness trade-off precisely where exoskeleton assistance—and delicate surgical manipulation—is most sensitive: near zero velocity and during frequent direction changes. In a surgical context, mitigating stick-slip phenomena and unmodeled friction in these low-speed regimes is critical for maintaining haptic transparency and ensuring the surgeon receives accurate force feedback during tissue interactions. Current limitations include slow thermal drifts and operating-point dependencies that were not explicitly modeled. Future work will incorporate lightweight adaptation to track temperature effects, extend testing to multi-task and contact scenarios, and integrate friction compensation and estimation within a unified low-impedance control scheme —ultimately broadening the impact of these estimation techniques from wearable exoskeletons to precision-critical medical robotics.

## Acknowledgment

This work was supported by the Italian Ministry of University and Research, under the complementary actions to the NRRP 'Fit4MedRob-Fit for Medical Robotics' Grant (# PNC0000007). This work was also partially funded by European Union - ERC-2023-SyG Endotheranostics (n. 101118626).

## References

[1] N. Moscatelli, C. Brambilla, V. Lanzani, and A. Scano, "Assessing Transparency of Robots, Exoskeletons, and Assistive Devices: A Systematic Review," Sensors, vol. 25, no. 14, 4444, 2025.

[2] C. Canudas-de-Wit, H. Olsson, K. J. Åström, and P. Lischinsky, "A new model for control of systems with friction," IEEE Trans. Autom. Control, vol. 40, no. 3, pp. 419–425, 1995.

[3] T. Xun, J. Yang and H. Ding, "Improving Robotic Grinding Force Control Precision: Nonlinear Friction Compensation Based on a Novel Continuous Dynamic Model," IEEE/ASME Transactions on Mechatronics, vol. 1, no. 1, pp. 1–12, 2024.

[4] L. Le-Tien, A. Albu-Schäffer, A. De Luca, and G. Hirzinger, "Friction observer and compensation for control of robots with joint torque measurement," in Proc. IEEE/RSJ Int. Conf. Intelligent Robots and Systems (IROS), 2008, pp. 3786–3793.

[5] E. Sariyildiz and K. Ohnishi, "Disturbance observer-based robust control and its applications: 35th anniversary overview," IEEE Trans. Ind. Electron., vol. 67, no. 3, pp. 2042–2053, 2019.

[6] S. Shan and Q. -C. Pham, "Sensorless Estimation of Contact Using Deep-Learning for Human-Robot Interaction," in Proc. IEEE Int. Conf. Robotics and Automation (ICRA), Yokohama, Japan, 2024, pp. 12935-12941.

[7] S. Haddadin, A. De Luca, and A. Albu-Schäffer, "Robot collisions: A survey on detection, isolation, and identification," IEEE Trans. Robot., vol. 33, no. 6, pp. 1292–1312, 2017.

[8] S. Long, X. Dang, and A. Gui, "Robot collisions: A novel sliding mode momentum observer for collaborative robot collision detection," Machines, vol. 10, no. 1, 818, 2022.

[9] J. A. Moreno and M. Osorio, "A Lyapunov approach to second-order sliding mode controllers and observers," in Proc. IEEE Conf. Decision and Control (CDC), 2008, pp. 2856–2861.

[10] G. Garofalo, N. Mansfeld, J. Jankowski, and C. Ott, "Sliding mode momentum observers for estimation of external torques and joint acceleration," in Proc. IEEE Int. Conf. Robotics and Automation (ICRA), 2019, pp. 6117–6123.

[11] J. Zhang, J. Wang, W. Li, J. Wang, and P. Yang, "Extended state observer-based sliding mode control design of two-DOF lower limb exoskeleton," Actuators, vol. 12, no. 11, p. 402, 2023.

[12] H. Khamar and M. Edrisi, "Designing a backstepping sliding mode controller for an assistant human knee exoskeleton based on nonlinear disturbance observer," Mechatronics, vol. 54, pp. 121–132, 2018.

[13] N. Masud, "Disturbance observer based dynamic load torque compensation for human-exoskeleton system," M.S. thesis, Univ. Gävle, Sweden, 2018.